Polar Research

RESEARCH/REVIEW ARTICLE

The first magnetotelluric image of the lithospheric-scale geological architecture in central Svalbard, Arctic Norway

Thomas I. Beka,[1] Maxim Smirnov,[2] Steffen G. Bergh[3] & Yngve Birkelund[1]

[1] Department of Physics and Technology, University of Tromsø, Norway, P.O. Box 6050 Langnes, NO-9037 Tromsø, Norway
[2] Oulu Mining School, Geophysics, University of Oulu, P.O. Box 3000, FI-90014 Oulu, Finland
[3] Department of Geology, University of Tromsø, Norway, P.O. Box 6050 Langnes, NO-9037 Tromsø, Norway

Keywords
Magnetotellurics; 2D modelling; lithosphere architecture; geothermal; Svalbard.

Correspondence
Thomas I. Beka, Department of Physics and Technology, University of Tromsø, P.O. Box 6050 Langnes, NO-9037 Tromsø, Norway.
E-mail: thomas.beka@uit.no

Abstract

Magnetotelluric data, collected from 30 stations on Spitsbergen as part of a reconnaissance geothermal resource assessment along a profile with 0.5–3-km spacing in 0.003–1000-s period range, were used to develop a lithospheric-scale two-dimensional (2D) resistivity model, heretofore unavailable for the region. Inverting the determinant of the impedance tensor in 2D, we found the smoothest model fitting the data within a specified tolerance level. We justified the model by perturbing it, performing sensitivity analysis and re-running the inversion with a different algorithm and starting models. From our final model, we constructed a crustal-scale stratigraphic framework, using it to estimate the depth of major geological features and to locate structural deformations. The 2D resistivity model indicates a shallow low resistive (<100 Ωm) Paleozoic–Mesozoic sedimentary sequence, varying laterally in thickness (2–4 km), obstructed by a gently dipping Permian–Carboniferous succession (>1000 Ωm) east of the Billefjorden Fault Zone. Underneath, a (possibly Devonian) basin is imaged as a thick conductive anomaly stretching >15 km downwards. Beneath a deformed Paleozoic–Mesozoic successions, an uplifted pre-Devonian shallow basement (>3000 Ωm) is revealed. We estimated a thin lithosphere, in the range of ca. 55–100 km thick, that could explain the area's elevated surface heat flow (ca. 60–90 mW/m^2), consistent with the calculated depth of thermal lithosphere heat-base boundaries for a partially melting mantle. The model indicates a possible replenishment pathway of upward heat transport from the shallow convective mantle to the composite crustal conductive units. This is encouraging for low-enthalpy geothermal development.

Human settlements in the Arctic region of Svalbard, originally established as mining communities, are experiencing increasing traffic driven mainly by tourism and research. In line with this, energy demands are growing, potentially adding pressure on the fragile Arctic environment, which is already feeling effects of rising global temperatures.

To mitigate local emissions, trapping CO_2 from its source in the settlement of Longyearbyen and storing it underneath the surface in the adjacent valley of Adventdalen (Fig. 1c) is being considered. To better understand the structure of the targeted reservoir (ca. 670–970 m below the surface), a CO_2 borehole park—the Longyearbyen CO_2 Lab's well park (LCOP; Fig. 1c) consisting of several deep wells—was established to study the subsurface structure (Braathen et al. 2012). Recently, parallel to the LCOP project, interest in investigating the geothermal potential has been instigated by the archipelago's documented thermal springs and recent volcanism (Harland 1997; Pascal et al. 2011).

Svalbard's high thermal potential is largely linked to its proximity to a transform tectonic margin. The heat-flow rate in the region is considerably larger than what is commonly found in northern Europe (Khutorskoi et al. 2009; Slagstad et al. 2009). For instance, 130 mW/m^2 is recorded in an area believed to be affected by a late

Citation: *Polar Research* 2015, *34*, 26766, http://dx.doi.org/10.3402/polar.v34.26766

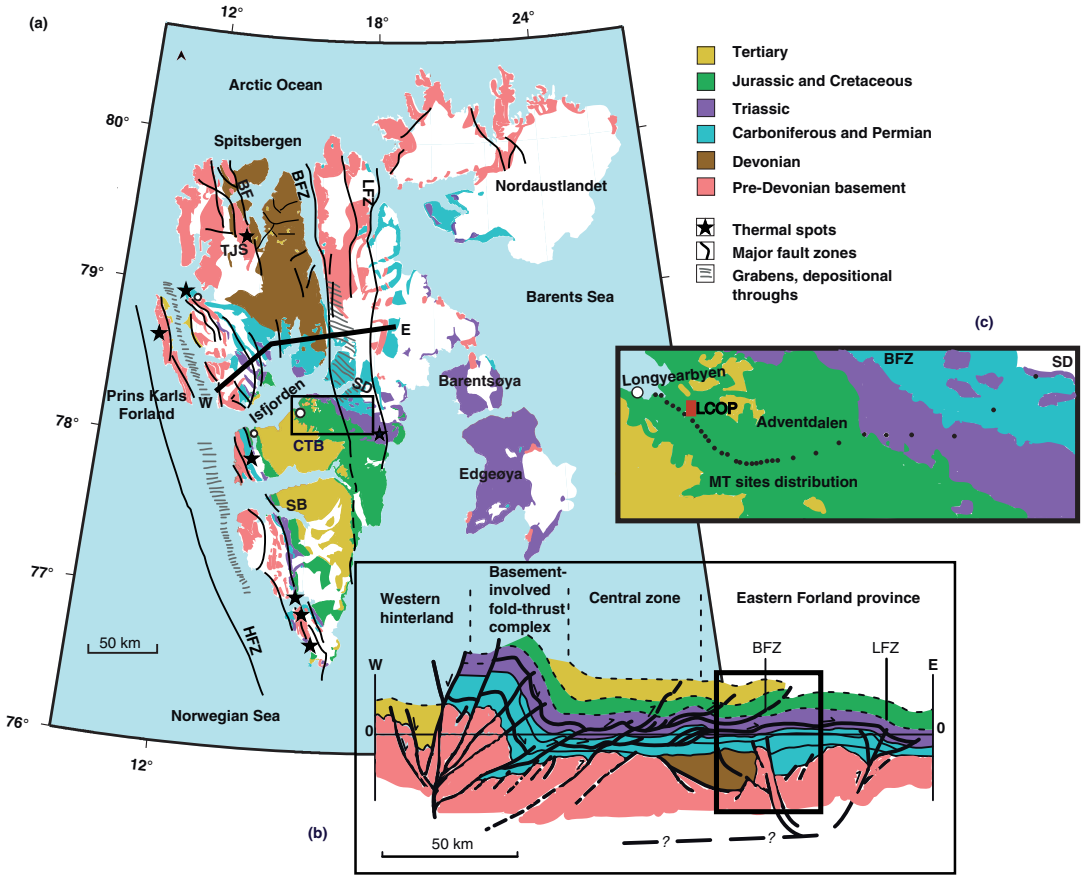

Fig. 1 (a) Geo-tectonic map of Svalbard redrawn from Dallmann et al. (2002). (b) Schematic regional scale cross-section in a west–east transect across north–central Spitsbergen redrawn from Bergh & Grogan (2003). The portion of the cross-section that is marked by a rectangle corresponds to the magnetotelluric (MT) result shown in Fig. 3b. (c) Station distribution for the measured MT profile, indicated by the rectangle in (a). Geological and other features are abbreviated as follows: Lomfjorden Fault Zone (LFZ); Billefjorden Fault Zone (BFZ); Breibogen Fault (BF); Hornsund Fault Zone (HFZ); the warm springs Trollkildene and Jotunkildene (TJS); Central Tertiary Basin (CTB); Sysselmannbreen (SB); Sassendalen (SD); Longyearbyen CO_2 Lab's well park (LCOP).

Cenozoic crustal uplift (Vågnes & Amundsen 1993), and more recently 80 mW/m^2 is reported as a steady borehole heat-flow rate in the Sysselmannbreen area (Fig. 1a) of central Spitsbergen (Pascal et al. 2011). Borehole studies have also indicated thermal gradients surpassing 40°C/km beneath the permafrost in the LCOP area (Elvebakk 2010). Adjacent to a Quaternary age volcanic system on Spitsbergen are the northernmost documented thermal springs in the world: Trollkildene and Jotunkildene (Fig. 1a), lying along the north–south trending Breibogen Fault (Fig. 1a; Banks et al. 1998; Treiman 2012). Other discovered thermal fields (Fig. 1a) are linked to a network of major north–south trending fault zones that are parallel to the Cenozoic Hornsund–DeGeer Fault Zone transform plate boundary, just west of Spitsbergen (Dallmann 1999; Faleide et al. 2008).

The list of major faults on Svalbard includes, among others, the Billefjorden Fault Zone (BFZ) and Lomfjorden Fault Zone (Harland 1997; Dallmann 1999; Bælum & Braathen 2012), which bound segmented block architectures. Most of the present-day major fault systems were formed in the Caledonian through Paleozoic era but were later reactivated as compressive faults in the Paleocene–Eocene period (Bergh et al. 1997; Harland 1997), causing extensive uplift and exhumation in certain domains. Besides the widespread fault systems, it is not uncommon to register notable seismic incidents in the Svalbard region (Mitchell et al. 1990; Pirli et al. 2010).

The stratigraphy of Svalbard is that of a crystalline and metamorphic basement of Precambrian and Caledonian rocks overlain by a thick composite sedimentary sequence starting with Devonian and Carboniferous basin fills, and successive Permian through Eocene platform deposits up to 3.5 km in thickness (Harland 1997; Dallmann et al. 2002). Notable thickness variations exist in the west–central and eastern parts of Svalbard for the Devonian

Citation: *Polar Research* 2015, *34*, 26766, http://dx.doi.org/10.3402/polar.v34.26766

and Carboniferous basin deposits and also for strata adjacent to the major reactivated block–boundary faults such as the BFZ and the Lomfjorden Fault Zone (Harland 1997).

The presence of a well-established geolithological and structural framework makes the Svalbard region suitable for magnetotelluric (MT) and other geophysical studies. Apart from this, the remoteness of the area from signal corrupting industrial noise makes the archipelago well suited for carrying out a natural-source MT study. On the other hand, the nearness of ionospheric sources may distort the MT data at such latitudes (Viljanen et al. 1999; Simpson & Bahr 2005; Chave & Jones 2012). However, in our case, the depth of interest is much smaller than the closest distance (ca. 100–120 km) to the source. Therefore, the plane wave condition for the depth of interest should be satisfactory.

Fieldwork was carried out in August 2013 and May 2014 in a glacial valley that comprises a large fluvial plain between Longyearbyen and the valley of Sassendalen (Fig. 1a, c). During the short ice- and snow-free summer, the valley is covered by tundra vegetation. Underneath the surface, the ground is sealed by permafrost, with thicknesses varying from the coast to inland as well as from low- to highland areas. The area is considered to be promising for a geothermal resource exploration because of its proximity to the BFZ, the presence of a crustal Devonian graben and a history of anomalous heat flow. In addition to the geotectonic factors, propinquity of the area to the energy demand and local infrastructure were important considerations in our decision to carry out the study at the specified location.

In this paper, we present results of the MT survey and show the first lithospheric-scale two-dimensional (2D) resistivity model of the area. We compare our results with previous geological studies (Amundsen et al. 1987; Vågnes & Amundsen 1993; Eiken 1994; Lamar & Douglass 1995; Bergh et al. 1997; Dallmann et al. 2002; Bergh & Grogan 2003; Bælum et al. 2012; Blinova et al. 2012) and use them to construct crustal level geological stratigraphy and lithospheric architecture, estimate the depth of major geological features and, finally, make a reconnaissance geothermal prospect assessment of the area.

Methods

MT is a geophysical method for deriving subsurface resistivity structures from measured naturally occurring Earth's electromagnetic (EM) fields at the surface (Tikhonov 1950; Cagniard 1953). From the measured EM time-series data, a 2×2 impedance tensor (Z) is estimated (Berdichevsky 1960), which links the measured horizontal components of the electric ($Eh = [E_x, E_y]$) and magnetic ($H_h = [H_x, H_y]$) fields in frequency domain as $E_h = ZH_h$, where

$$Z = \begin{bmatrix} Z_{xx} & Z_{xy} \\ Z_{yx} & Z_{yy} \end{bmatrix}. \quad (1)$$

Apparent resistivity (ρ) and phase (φ) parameters are estimated from the complex Z tensor and used to reconstruct subsurface resistivity. In addition, Z contains information about the underlying data geoelectric and dimensionality structure, whose analyses are necessary to justify the routinely used 2D field data inversion with a suitable numerical algorithm.

MT has a wide range of applications both in shallow crustal resource exploration and deep earth studies. In particular, MT is favoured for geothermal resource exploration (Spichak & Manzella 2009) on account of the interrelationship between subsurface electrical properties and geothermal attributes such as fluid content, porosity and temperature. Producing little impact on the environment, MT is well suited for application in fragile areas like the Svalbard tundra.

The data we present were collected at 30 MT sites distributed along a profile of ca. 30 km in length, with stations spaced every 500–3000 m. For logistical reasons, the distance between stations was not homogeneous. All-terrain vehicles are prohibited on the tundra, with the exception—when there is snow—of snowmobiles. We therefore collected data in the eastern part of the profile, which lacked road access, while there was still snow cover and when the temperature was not much below the freezing point, as very cold temperatures impede instrument functioning. These practical constraints led to larger station-to-station distances in the eastern, as compared to the western, part of the profile (Fig. 1c).

For data recording, we used the MTU2000 system, developed at Uppsala University in Sweden for broadband MT measurement in the 0.003–1000-s period range (Smirnov et al. 2008). Contributing to the high quality of the data is the site's remoteness from industrial noise. We have not noticed any irregularity in the quality of the collected broadband data that we can relate to the source field effects.

The measured time-varying electric and magnetic field data were processed using the robust remote reference algorithm of Smirnov (2003), where the final result is derived by averaging multiple remote reference estimates in a robust statistical manner (Smirnov & Pedersen 2009).

When resistivity of the underlying medium is of a 2D character, that is, if a principal regional strike direction is present, the structure of the impedance tensor (Eqn. 1) becomes simpler and only the off-diagonal elements have

values that are significantly different from zero when the tensor is rotated along the strike direction. In our case, a regional N30°E strike direction was identified, with 90° ambiguity (Simpson & Bahr 2005; Chave & Jones 2012), using Bahr's phase-sensitive (Bahr 1991) and Q-function (Zhang et al. 1987; Smirnov & Pedersen 2009) methods as dimensionality tools (Fig. 2a, b). The presence of a principal Z direction, where the tensor is reduced to its off-diagonal elements, implying one horizontal direction where resistivity is constant, gives a ground to interpret the data in 2D.

On the other hand, large Bahr's phase-sensitive three-dimensional (3D)/2D skew (Bahr 1988) parameters were identified for a fraction of the data (Fig. 2c), despite the clear regional strike behaviour discussed above. The purpose of this dimensionless and rotationally invariant parameter is to investigate the extent of 3D in the impedance tensor. A skew that is larger than 0.3 may indicate a 3D effect (Bahr 1991; Ledo et al. 2002), although the opposite

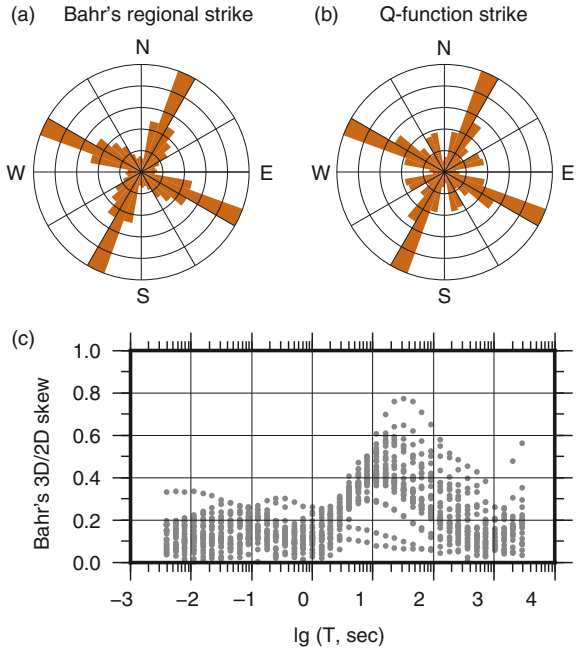

Fig. 2 The dominant regional level geoelectric strike direction with 90° ambiguity and Bahr's three-dimensional/two-dimensional (3D/2D) skew for all the measured 30 stations and the entire measured period range (0.003–1000 s) in $\log_{10}$ (lg) scale. (a) Rose diagram illustrating a regional N30°E geoelectric direction estimated through Bahr's phase-sensitive method. (b) For comparison, a rose diagram displaying a dominant regional strike (N30°E) estimated through the Q-function method, is shown. (c) Bahr's 3D/2D skew parameter as a function of the measured periods. Station-wise data skew parameters (y axis) larger than the empirical threshold of 0.3 may indicate a possible 3D effect, which makes 2D determinant inversion preferable for data interpretation.

(<0.3) is in general not sufficient but necessary to justify a 2D geoelectric structure (Ledo et al. 2002). In our case, 3D effects were indicated at most of the measured sites as large skews ranging between 0.3 and 0.7. In particular, the 3D effects were notable in the ca. 10–100-s period range (Fig. 2c). Therefore, in order to ease the 3D concern raised by the large skews, we found employing the determinant of the impedance tensor reasonable rather than utilizing the bi-modal (TE+TM) data jointly as input for 2D inversion. The determinant of the impedance tensor is advocated for its robust behaviour during a 2D inversion in a 3D environment and is favoured for its invariant property under rotation (Pedersen & Engels 2005).

Next, we carried out a 2D interpretation of the data in Occam's manner (Constable et al. 1987) using the electro-magnetic inversion with least intricate algorithm (EMILIA; Kalscheuer et al. 2010). This code is well suited for trying out various smoothness-constraint settings (Cherevatova et al. 2014), which we took advantage of during the early stages of our inversion experiments. For consistency, results obtained from the EMILIA inversion were carefully compared against outputs of the reduced data space Occam (REBOCC) inversion (Siripunvaraporn & Egbert 2000).

Within Occam's inversion strategy, we attempted to find the smoothest model that fits the observed data. The goal in this case was reaching one as a root mean square (RMS) misfit between the observed and predicted data, while fitting the data within a specified error floor and data errors. We carried out such an inversion on the apparent resistivity and phase parameters. For each station, 36 frequency points were included. Inversion was started with a 100-Ωm half-space model with 128×101 parameter size. To ensure correct model scaling, sites were projected onto a profile perpendicular to the chosen strike (N30°E). During model regularization, equal vertical and horizontal weights were given. By assuming a 5% data error floor for both the apparent resistivity and phase parameters, we ran the inversion and obtained at the fourth iteration a model that fit the data with 1.06 misfit RMS. This model is presented as the preferred model of interpretation in Fig. 3a. Pseudo-sections of the misfit between the observed and predicted data of the final model are displayed in Fig. 4. In general, the figure indicates a good data fit without any particular over-fitted or under-fitted sections. The geometry of anomalies of interest in the final model seems to agree well with other models obtained when, as a test, we repeated the inversion procedure using REBOCC and other starting models. As an example, we present a result from one of these test inversions (Fig. 5) to demonstrate consistency and as a comparison to the final model.

Citation: *Polar Research* 2015, *34*, 26766, http://dx.doi.org/10.3402/polar.v34.26766

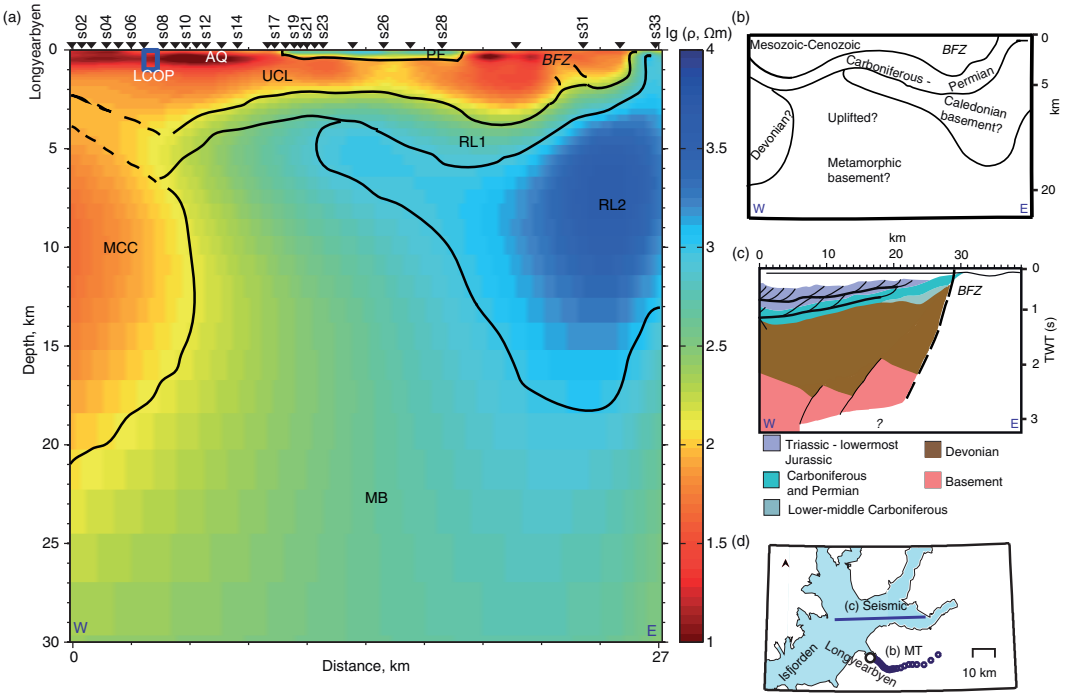

Fig. 3 (a) The final two-dimensional (2D) magnetotelluric (MT) model. The colour scale (lg) is shown in $\log_{10}$. An error floor of 5% is assigned on the inverted data, and the inversion is started from a 100-Ωm half-space model. The data misfit of the final model is shown in Fig. 4. (b) Geological interpretation of the MT model. (c) A schematic geological cross-section derived from a seismic section (parallel to the MT profile) in eastern Isfjorden, redrawn from Blinova et al. (2012). The y axis is given in two-way-travel time (TWT, s), where each second represents two-way-travel time (see Blinova et al. 2012). (d) The offshore seismic transect and the measured MT sites are shown in the same map to illustrate the position of the two profiles in relation to each other. Isfjorden is indicated to facilitate comparison with Fig. 1. The MT result is comparable to interpretations derived from seismic sections as in (c) and to the stratigraphic section marked by the rectangle in Fig. 1b. Geological and other features are abbreviated as follows: Longyearbyen CO_2 Lab's well park (LCOP); permafrost (PF); upper-crust conductive layer (UCL); mid-crust conductor (MCC); resistive layer 1 (RL1); resistive layer 2 (RL2); metamorphic basement (MB).

Results

The resistivity geometry we obtained from the 2D resistivity model seems to reflect the geological framework previously identified in seismic studies (Eiken 1994; Bergh et al. 1997; Bergh & Grogan 2003; Bælum & Braathen 2012; Blinova et al. 2012) and by surficial geology (Haremo & Andresen 1992; Lamar & Douglass 1995; Harland 1997; Dallmann et al. 2002). We classify the main resistivity structures revealed in the final model (Fig. 3a) between surface and 30-km depth into six major categories.

(1) Along the middle part of the MT profile, a thin resistive anomaly is identified sealing the ground from the surface to the depth of ca. 200 m. This anomaly is interpreted as permafrost and displays a comparable thickness to what is considered to be normal in deglaciated valleys and coastal landscapes of Svalbard (Christiansen et al. 2010; Braathen et al. 2012).

(2) An upper-crust anomalous conductive composite (UCL) has resistivity values <100 Ωm and runs between Longyearbyen and the BFZ (Fig. 1a) for longer than 20 km. We interpret this shallow conductive anomaly as part of the extensive Paleozoic through Mesozoic basin–platform sequence (Bergh et al. 1997; Dallmann et al. 2002; Bælum & Braathen 2012) found in central Svalbard. The thickness of this structural anomaly varies laterally from 2 to 4 km, with the thickest portions linked to the LCOP and the region just west of the BFZ. The lateral variation in thickness can be due to a regional syncline dip of the strata in central Spitsbergen as well as the presence of thick Devonian and Carboniferous basins beneath the Mesozoic platform units. This is most pronounced adjacent to the BFZ (Maher & Braathen 2011; Bælum & Braathen 2012).

The near-surface (<1 km) section of the UCL has particularly low resistivity, which likely indicates an aquifer. The aquifer-like anomaly (AQ) is at its thickest near the LCOP, where the subsurface is considered as a potential CO_2 sequestration reservoir. The MT-inferred AQs are situated at a depth scale comparable with aquifers identified

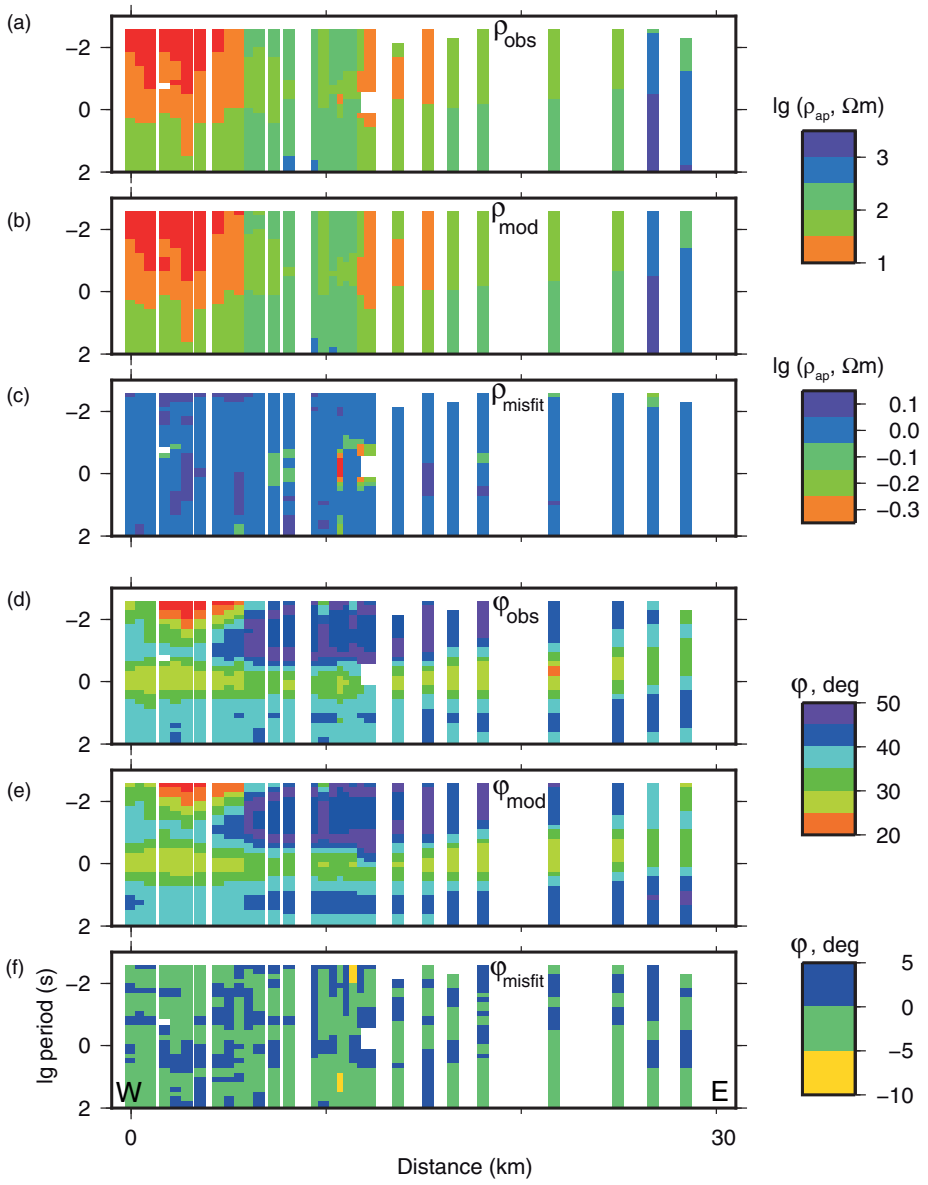

Fig. 4 Pseudo-sections of the misfit between the observed and predicted responses of the determinant data underlying the two-dimensional magnetotelluric model shown in Fig. 3. Sites are sorted in increasing order from left (west) to right (east). Apparent resistivity and period (y axis) are given in $\log_{10}$ (lg) scales, and phase is shown in degrees. The total misfit root mean square of the inversion is 1.06. (a) Observed apparent resistivity. (b) Predicted apparent resistivity. (c) Apparent resistivity misfit. (d) Observed phase. (e) Predicted phase. (f) Phase misfit.

through borehole methods (Bælum et al. 2012; Braathen et al. 2012). AQ reappears after being obstructed by the permafrost layer and is visible until it finally gets blocked by the BFZ from the east.

(3) A large conductive anomaly (mid-crust conductor, or MCC) is observed in the mid-crust region underneath the western portion of the profile. Unlike the laterally elongated UCL, this anomaly is vertically elongated, extending from ca. 4 to >15 km depth below the surface. In order to investigate a possible effect on the MCC, we included the nearby ocean and fjord system into the modelling. We did so by utilizing the bathymetry of the region to determine the extent of oceanic water (0.3 Ωm) while preparing a priori model for the 2D inversion. Inversions that we ran with such a priori model revealed a similar MCC geometry as the one seen in the final model (Fig. 3a). This indicates that the MCC is required to fit the data regardless of the ocean. In addition, as a sensitivity

Citation: *Polar Research* 2015, *34*, 26766, http://dx.doi.org/10.3402/polar.v34.26766

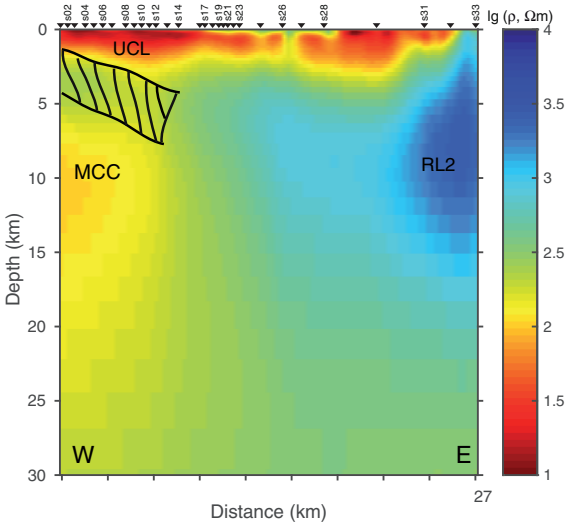

Fig. 5 A two-dimensional model example presented to show the reproducibility of the resistivity geometry seen in the final model (Fig. 3a). We obtained the model by re-running the inversion procedure using 1000-Ωm half space as a starting model with the reduced data space Occam algorithm. This model, which is obtained after eight iterations, has the data misfit root mean square 1.06. The hatched area between the upper-crust conductive layer (UCL) and the mid-crust conductor (MCC) indicates the section of the final model area we tested for sensitivity. The location of resistive layer 2 (RL2) is marked.

test, we replaced the MCC with a background resistivity of 500 Ωm and ran forward modelling by including the altered model as input. This led the data misfit to increase by a factor of three compared to the original final model's RMS, yielding 3.11 as a new misfit. This result again indicates reasonable data sensitivity to the MCC anomaly.

The bottom depth of the MCC cannot be precisely determined because of the MT's better response to conductive anomalies and on account of the smearing effect following the diffusive nature of propagating EM energy into the Earth (Simpson & Bahr 2005). The MCC anomaly, nevertheless, coincides reasonably well with the thick Devonian basin fill identified earlier in north central Spitsbergen underlying a Paleozoic–Mesozoic sequence and terminating abruptly west of the BFZ (Fig. 1a, b) (Bergh & Grogan 2003; Bælum & Braathen 2012). Seismic studies of the region (Bergh et al. 1997; Bergh & Grogan 2003) have indicated the Devonian unit having a regional asymmetric character along a west–east transect. The unit starts with a large surface manifestation west of the BFZ in the northern part of the island, before gently dipping southwards and getting overburdened by the late Paleozoic through Mesozoic successions (Fig. 1a). This accords with the MT model we present here.

(4) A laterally extended transfer zone between the shallow depth high conductive and a larger depth high resistive anomaly (RL1) is imaged east of the BFZ, overlying a rather deep and resistive anomalous object (RL2). The exposure of RL1 at the surface east of the BFZ coincides well with the Permian–Carboniferous sedimentary unit identified in the area on the surface (Fig. 1a) and dipping gently towards the west (Lamar & Douglass 1995; Bælum & Braathen 2012). Starting at the surface in the MT model, RL1 dips to the subsurface by approximately 45 degrees westward. In this way, after travelling a distance comparable to ca. 10 km along a horizontal direction, the resistive layer bends upwards, squeezing the Mesozoic sedimentary unit (UCL) above a décollement surface. The model indicates RL1 continuing westward (dashed lines in Fig. 3a) as a blurry, narrowly sandwiched gap between the UCL and the MCC.

A comparable but somewhat clearer resistive gap between the UCL and the MCC is suggested by the REBOCC inversion result (Fig. 5). However, because of the smearing effect, it is in general difficult to image a thin resistive layer and a sharp boundary using MT, especially when the structure is sandwiched between conductive parts (Constable et al. 1987). Therefore, to minimize the temptation to over-interpret, we performed a sensitivity test on the final model to determine whether the data resolution was enough to image the gap.

For test purposes, we modified the final model in two ways. As a first test model, we decreased the resistivity of the final inversion model in the test area from ca. 70–100 Ωm to 50 Ωm. The purpose is creating a better resemblance to the adjacent conductive anomalies, the UCL and the MCC. As a second test model, we assigned 500 Ωm to match the background resistivity, RL1 in this case. We performed forward modelling on the two test cases and examined the implication of the modifications we undertook on data misfits, relative to the 1.06 misfit RMS of the original final model. The result of the sensitivity test indicated an increase in data misfit, in both cases. However, relative to the final model's misfit, the RMS increase in the first test case was slightly larger (1.19) than in the second (1.12), despite the relatively smaller change made during the former (a 20-Ωm decrease from the original ca. 70–100 Ωm). Therefore, taking into account the high data quality, we conclude that the data suggest a gap between the UCL and the MCC.

(5) There is a clear increase in resistivity from RL1's ca. 1000 to RL2's >3000 Ωm. The latter has a vertically elongated elliptic shape that stretches from the near surface down to >15 km depth and branches out diagonally westward. As comparison between the forms of RL2 in Figs. 3a and 5 reveals, the exact shape of the anomaly can be difficult to determine, and its shape can vary following a minor modification in the inversion setting.

The problem may not be surprising considering MT's weak response to resistive anomalies, especially at greater depth. However, the absence of a strong conductor beneath RL2 as well as model regularization parameters may have contributed to the unreliable RL2 structure. Nevertheless, based on the distinctive resistivity behaviour and geometry of RL2, we interpreted the anomaly as an upthrusted Caledonian basement block. Such interpretation seems reasonable in the context of a known basement uplift east of the BFZ (Haremo & Andresen 1992), which may have led to the upward bent in the overlaying Paleozoic sequence (RL1).

(6) The semi-resistive anomaly that covered most of the deeper crust is interpreted as a Pre-Cambrian basement metamorphic rock. Although the basement metamorphic rock shows dominance in the middle and lower crust, there are instances where the basement appears at much shallower depth (<3 km), for instance in the subsurface region located under the sites s14–s21.

On a larger scale, the resistivity model reflects a complicated geological architecture. The interaction between the resistive layers (RL1, RL2 and the basement metamorphic rock) and the UCL in the upper crust accounts for the lacking lateral and vertical structural continuity in central Spitsbergen, a phenomenon previously seen on surface geology and seismic sections (Bergh et al. 1997). Beneath the permafrost sealed profile section, the UCL is squeezed upwards by the basement uplift (RL2). Compared to the adjoining basement metamorphic rock and the MCC, which are more conductive, permeability in RL2 to up-welling heat may be more limited because of the nature of the Caledonian basement structure. This may have reduced the amount of heat arriving to the near surface in the profile section, eventually obstructing the AQ and making conditions favourable for the formation of a strong permafrost layer.

In Fig. 6, we present the lithosphere through upper asthenosphere resistivity stratigraphy in one-dimension by averaging the 2D model down to a large depth. The figure shows a regional level resistivity, which tends to decrease steadily below the ca. 30-km semi-resistive Moho depth (Faleide et al. 2008). Resistivity drops to ca. 250 Ωm at around 55 km, a depth scale equivalent to a previously estimated regional level lithosphere thickness on the Svalbard platform (Vågnes & Amundsen 1993) based on xenolith data (Amundsen et al. 1987). The highly conductive upper mantle between 55 and 100 km below the surface is interpreted as a transitional zone from lithosphere to electric-asthenosphere (ca. 10–100 Ωm; Karato 1990). For comparison, we computed the depth at which mantle materials start partially melting (i.e., top of the electrically conductive asthenosphere L in km) using a simple power law correlation under the assumption that the thermally defined lithosphere base follows the 1300°C isoline (Artemieva 2006); given that surface heat flow (Q) is known and is reasonably large (>50 mW/m^2) as is often the case in most non-cratonic regions (O'Reilly & Griffin 1996; Artemieva 2006):

$$\mathrm{L} = 418\ \mathrm{e} - 0.023\mathrm{Q}. \quad (2)$$

It is convincing that the geological context of Svalbard—along an ocean–continent transform margin with active tectonism, recent volcanism and documented thermal springs (Harland 1997; Pascal et al. 2011)—makes the power law applicable for our purpose.

A heat-flow study in the LOCP borehole (along the MT profile; Fig. 1c) has reported heat flow rates that in general tend to vary between 60 and 90 mW/m^2 (Pascal et al. 2011). According to Eqn. 2, a surface heat flow level of 60 and 90 mW/m^2 is required to obtain a partially melting mantle at ca. 105 and 53 km below the surface, respectively. And the uncertain depth scales for the partial mantle melt (the dashed lines of $Q=90$ and $Q=60$ in Fig. 6a) coincide well with what we proposed as a zone of electric lithosphere–asthenosphere boundary uncertainty (also on Fig. 6a). Finally, considering 100 Ωm as a typical upper boundary for asthenospheric resistivity, following Karato (1990) and references therein, we set the electric lithosphere–asthenosphere boundary (e-LAB; Jones 1999; Martinec & Wolf 2005; Korja 2007) at about 100 km below the surface. Furthermore, the resistivity geometry we presented in Fig. 6b suggests a link between the convective upper mantle and the subcrustal conductive structures. This link is interpreted as a possible passage of heat going upwards (Fig. 6b) from the convective mantle to the upper-crustal sedimentary units.

Discussion and conclusions

The new MT data help to extend the geological knowledge of Svalbard that has until now mostly been inferred from surficial, seismic and gravity data. Understanding the nature of the base of the lithosphere is important since the asthenosphere plays crucial roles when it comes to the geodynamics of the overlying lithosphere (O'Reilly & Griffin 1996; Jones 1999). The top of the asthenosphere can be estimated on the basis of electrical signatures retrieved from MT data (Martinec & Wolf 2005; Korja 2007). To serve such purposes, 10–100 Ωm is suggested as a realistic range of asthenospheric resistivity (Karato 1990). Our data indicated the upper boundary (100 Ωm) at ca. 100 km below the surface. However, it is unclear whether the actual transition to the asthenosphere occurs

Citation: *Polar Research* 2015, *34*, 26766, http://dx.doi.org/10.3402/polar.v34.26766

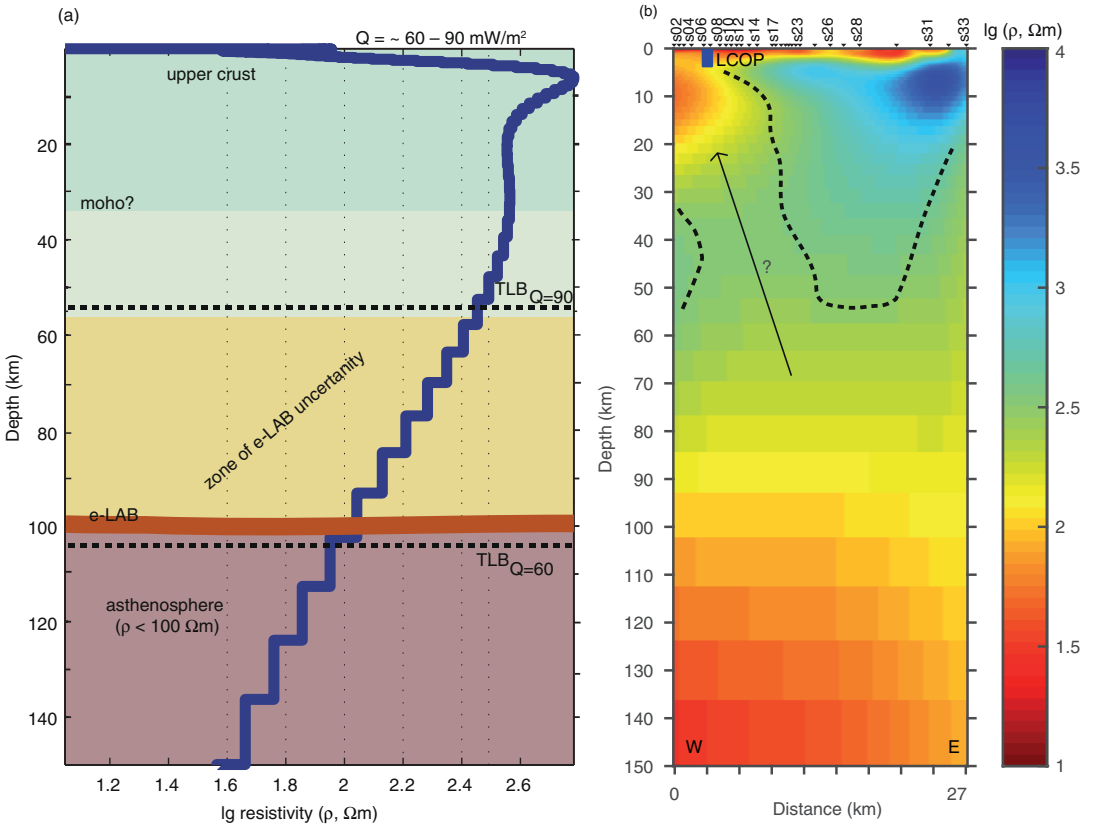

Fig. 6 Resistivity geometry from lithosphere through upper asthenosphere depth. Resistivity values are shown in $\log_{10}$ (lg) scale. (a) One-dimensional regional resistivity stratigraphy obtained from the averaged two-dimensional model shown in (b). Q is the measured surface heat-flow rate, which ranged in value from 60 to 90 mW/m^2 along the magnetotelluric (MT) profile (Pascal et al. 2011). The depth scale marked as the zone of electrical lithosphere–asthenosphere boundary (e-LAB) uncertainty falls within the calculated upper and lower thermal lithospheric base boundaries (calculated with Eqn. 2) with the specified Q. The Moho depth for Svalbard platform (ca. 30 km) is taken from Faleide et al. (2008). (b) The final two-dimensional MT model (Fig. 3) extended down to upper asthenospheric depth. The resistivity geometry marked by the arrow suggests a link between the crustal sedimentary units and the shallow convective mantle. The location of the Longyearbyen CO_2 Lab's well park (LCOP) is marked.

before reaching this depth (somewhere between 55 and 100 km), considering elevated conductivity ($<$250 Ωm) on a depth scale that would be relevant to asthenospheric conditions in the thermal and rheological context (Korja 2007) of the Svalbard platform (Vågnes & Amundsen 1993; Vogt & Sundvor 1996). This uncertainty has support from the calculation we made using Eqn. 2 to find the thermally defined 1300°C base of the lithosphere—the top of partial mantle melt (Artemieva 2006; Korja 2007)—based on measured surface heat-flow rates. Furthermore, the MT-estimated e-LAB is within the typical range of lithosphere thickness (90–120 km) in non-cratonic regions (O'Reilly & Griffin 1996). At the same time, 55 km as a proposed starting depth of transition to the asthenosphere agrees well with a previous lithosphere thickness estimate from xenolith data (Amundsen et al. 1987; Vågnes & Amundsen 1993). In terms of the crustal geotherm, if mantle is considered to contribute 60% of the surface heat flow (Pollack & Chapman 1977; Hatton 2009), proposing a thinned lithosphere would be in agreement with the elevated heat flow rates observed in various locations on Spitsbergen (Vågnes & Amundsen 1993; Vogt & Sundvor 1996; Pascal et al. 2011).

Permafrost is not resolved for a significant portion of the profile. This may seem questionable, although the thickness variation—or even absence in some coastal areas and valleys—of permafrost has been documented in Svalbard (Christiansen et al. 2010; Braathen et al. 2012). The stratigraphy of the upper 100 m in the LCOP area is dominated by Holocene gravel and sand layers (Bælum et al. 2012; Braathen et al. 2012) cemented by permafrost or, as our results indicated, filled with fluids of melted permafrost. In addition, the near-surface section of the studied fluvial plain may contain a large amount of

wet and conductive oceanic sediments capable of overriding permafrost, which otherwise would be resolved by MT as a resistive anomaly.

The final resistivity model that we present is robust, with a good data misfit (RMS = 1.06) and without any particular over- or under-fitted sections (Fig. 4). The reproducibility of the resistivity geometry is confirmed through various re-run inversion tests we made using different algorithms and starting models (Fig. 5). There is a good agreement between the presented MT model (Fig. 3a, b) and surficial geology (Fig. 1a, b) that makes our MT model attractive for further geological analysis. On a deeper level, the MT results coincide well with a parallel marine seismic model (Fig. 3c, d) obtained from a fjord north of the MT profile (Blinova et al. 2012).

The MT model provides information on the geological stratigraphy, depth scales and architecture of an area in central Svalbard. We found the downward thickness of a Devonian basin surpassing 15 km. A Caledonian basement, upthrusted and vertically elongated from the surface down to 17 km depth, is imaged underneath a deformed Paleozoic–Mesozoic succession. We identified a metamorphic basement extending to a shallow crustal depth mainly adjacent to the Devonian basin fill, and we inferred a thinned lithosphere from the MT data.

The presence of a thick near-surface composite conductive layer, often associated with a potential geothermal reservoir (Spichak & Manzella 2009), adjacent to Longyearbyen and a thinned lithosphere with a possible passage for upward heat transport invigorate the effort to find a geothermal source of energy in the region. Furthermore, the location of the subsurface, which MT indicated as holding a better heat prospect, lies underneath the carbon capture and sequestration (CCS) targeted area (Fig. 6b). This invites a better coupling between future CCS and geothermal projects in the area, since improved mobility due to low viscosity can be achieved from supercritical CO_2 ($ScCO_2$) as compared with water when used as a working fluid in a geothermal reservoir (Freifeld et al. 2013). To conclude, the presented 2D MT model helps to trace and compare sources of lateral and vertical structural discontinuities, including décollements previously inferred from surficial geology and seismic studies in central Svalbard.

Acknowledgements

The authors express their gratitude to the Norwegian Ministry of Foreign Affairs and the University of Tromsø for supporting the survey. The University of Oulu, Finland, is thanked for lending MT instruments. MS was funded by the Academy of Finland project 140988. We thank an anonymous reviewer and Björn Heincke, whose valuable comments and suggestions helped improve the manuscript. Finally, many useful discussions on MT with Maria Cherevatova, Uula Akseli Autio and Toivo Korja are appreciated.

References

Amundsen H.E.F., Griffin W.L. & O'Reilly S.Y. 1987. The lower crust and upper mantle beneath northwestern Spitsbergen: evidence from xenoliths and geophysics. *Tectonophysics 139*, 169–185.

Artemieva I.M. 2006. Global 1 × 1 thermal model TC1 for the continental lithosphere: implications for lithosphere secular evolution. *Tectonophysics 416*, 245–277.

Bælum K. & Braathen A. 2012. Along-strike changes in fault array and rift basin geometry of the Carboniferous Billefjorden Trough, Svalbard, Norway. *Tectonophysics 546*, 38–55.

Bælum K., Johansen T.A., Johnsen H., Rød K., Ruud B.O. & Braathen A. 2012. Subsurface structures of the Longyearbyen CO_2 Lab study area in central Spitsbergen (Arctic Norway), as mapped by reflection seismic data. *Norwegian Journal of Geology 92*, 377–389.

Bahr K. 1988. Interpretation of the magnetotelluric impedance tensor: regional induction and local telluric distortion. *Journal of Geophysics 62*, 119–127.

Bahr K. 1991. Geological noise in magnetotelluric data: a classification of distortion types. *Physics of the Earth and Planetary Interiors 66*, 24–38.

Banks D., Sletten R.S., Haldorsen S., Dale B., Heim M. & Swensen B. 1998. The thermal springs of Bockfjord, Svalbard: occurrence and major ion hydrochemistry. *Geothermics 27*, 445–467.

Berdichevsky M. 1960. Principles of magnetotelluric profiling theory. *Applied Geophysics 28*, 70–91.

Bergh S.G., Braathen A. & Andresen A. 1997. Interaction of basement-involved and thin-skinned tectonism in the Tertiary fold–thrust belt of central Spitsbergen, Svalbard. *American Association of Petroleum Geologists Bulletin 81*, 637–661.

Bergh S.G. & Grogan P. 2003. Tertiary structure of the Sorkapp–Hornsund region, south Spitsbergen, and implications for the offshore southern extension of the fold–thrust belt. *Norwegian Journal of Geology 83*, 43–60.

Blinova M., Faleide J.I., Gabrielsen R.H. & Mjelde R. 2012. Seafloor expression and shallow structure of a fold-and-thrust system, Isfjorden, west Spitsbergen. *Polar Research 31*, article no. 11209, doi: http://dx.doi.org/10.3402/polar.v31i0.11209

Braathen A., Baelum K., Christiansen H.H., Dahl T., Eiken O., Elvebakk H., Hansen F., Hanssen T.H., Jochmann M., Johansen T.A., Johnsen H., Larsen L., Lie T., Mertes J., Mørk M.B., Nemec W., Snorre O., Oye V., Rød K., Titlestad G.O., Tveranger J. & Vagle K. 2012. The Longyearbyen CO_2 Lab of Svalbard, Norway—initial assessment of the

geological conditions for CO_2 sequestration. *Norwegian Journal of Geology 92*, 353–376.

Cagniard L. 1953. Basic theory of the magnetotelluric method of geophysical prospecting. *Geophysics 18*, 605–635.

Chave A.D. & Jones A.G. 2012. *The magnetotelluric method: theory and practice*. Cambridge: Cambridge University Press.

Cherevatova M., Smirnov M., Korja T., Kaikkonen P., Pedersen L., Hübert J., Kamm J. & Kalscheuer T. 2014. Crustal structure beneath southern Norway imaged by magnetotellurics. *Tectonophysics 628*, 55–70.

Christiansen H.H., Etzelmüller B., Isaksen K., Juliussen H., Farbrot H., Humlum O., Johansson M., Ingeman-Nielsen T., Kristensen L., Hjort J., Holmlund P., Sannel A.B.K., Sigsgaard C., Åkerman H.J., Foged N., Blikra L.H., Pernosky M.A. & Ødegard R.S. 2010. The thermal state of permafrost in the Nordic area during the International Polar Year 2007–2009. *Permafrost and Periglacial Processes 21*, 156–181.

Constable S.C., Parker R.L. & Constable C.G. 1987. Occam's inversion: a practical algorithm for generating smooth models from electromagnetic sounding data. *Geophysics 52*, 289–300.

Dallmann W.K. 1999. *Lithostratigraphic lexicon of Svalbard*. Tromsø: Norwegian Polar Institute.

Dallmann W.K., Ohta Y., Elvevold S. & Blomeier D. 2002. *Bedrock map of Svalbard and Jan Mayen. Temakart 33*. Tromsø: Norwegian Polar Institute.

Eiken O. (ed.) 1994. *Seismic atlas of western Svalbard. Norsk Polarinstitutt Meddelelser 130*. Oslo: Norwegian Polar Institute.

Elvebakk H. 2010. *Results of borehole logging in well LYB CO_2, Dh4 of 2009, Longyearbyen, Svalbard*. Trondheim: Geological Survey of Norway.

Faleide J.I., Tsikalas F., Breivik A.J., Mjelde R., Ritzmann O., Engen O., Wilson J. & Eldholm O. 2008. Structure and evolution of the continental margin off Norway and the Barents Sea. *Episodes 31*, 82.

Freifeld B., Zakim S., Pan L., Cutright B., Sheu M., Doughty C. & Held T. 2013. Geothermal energy production coupled with CCS: a field demonstration at the SECARB Cranfield Site, Cranfield, Mississippi, USA. *Energy Procedia 37*, 6595–6603.

Haremo P. & Andresen A. 1992. Tertiary d'ecollement thrusting and inversion structures along Billefjorden and Lomfjorden fault zones, east central Spitsbergen. In R.M. Larsen (ed.): *Structural and tectonic modelling and its application to petroleum geology*. Pp. 481–494. Amsterdam: Elsevier.

Harland W.B. 1997. *The geology of Svalbard*. London: Geological Society of London.

Hatton C. 2009. Geotherms, lithosphere thickness and sedimentary basins. In: *Abstracts. The South African Geophysical Association 2009 Biennial Technical Meeting and Exhibition "Ancient Rocks to Modern Techniques."* Pp. 217–220. Gardenview: South African Geophysical Association.

Jones A.G. 1999. Imaging the continental upper mantle using electromagnetic methods. *Developments in Geotectonics 24*, 57–80.

Kalscheuer T., Juanatey M.D.l.Á.G., Meqbel N. & Pedersen L. B. 2010. Non-linear model error and resolution properties from two-dimensional single and joint inversions of direct current resistivity and radiomagnetotelluric data. *Geophysical Journal International 182*, 1174–1188.

Karato S. 1990. The role of hydrogen in the electrical conductivity of the upper mantle. *Nature 347*, 272–273.

Khutorskoi M., Leonov Y.G., Ermakov A. & Akhmedzyanov V. 2009. Abnormal heat flow and the troughs nature in the northern Svalbard plate. *Doklady Earth Sciences 424*, 29–35.

Korja T. 2007. How is the European lithosphere imaged by magnetotellurics? *Surveys in Geophysics 28*, 239–272.

Lamar D.L. & Douglass D.N. 1995. *Geology of an area astride the Billefjorden Fault Zone, northern Dicksonland, Spitsbergen, Svalbard. Skrifter 197*. Oslo: Norwegian Polar Institute.

Ledo J., Queralt P., Martí A. & Jones A.G. 2002. Two-dimensional interpretation of three- dimensional magnetotelluric data: an example of limitations and resolution. *Geophysical Journal International 150*, 127–139.

Maher H. & Braathen A. 2011. Løvehovden fault and Billefjorden rift basin segmentation and development, Spitsbergen, Norway. *Geological Magazine 148*, 154–170.

Martinec Z. & Wolf D. 2005. Inverting the Fennoscandian relaxation-time spectrum in terms of an axisymmetric viscosity distribution with a lithospheric root. *Journal of Geodynamics 39*, 143–163.

Mitchell B., Bungum H., Chan W. & Mitchell P. 1990. Seismicity and present-day tectonics of the Svalbard region. *Geophysical Journal International 102*, 139–149.

O'Reilly S.Y. & Griffin W.L. 1996. 4-D lithosphere mapping: methodology and examples. *Tectonophysics 262*, 3–18.

Pascal C., Balling N., Barrere C., Davidsen B., Ebbing J., Elvebakk H., Mesli M., Roberts D., Slagstad T. & Willemoes-Wissing B. 2011. *HeatBar final report 2010. Basement heat generation and heat flow in the western Barents Sea—importance for hydrocarbon systems. Technical report*. Trondheim: Geological Survey of Norway.

Pedersen L.B. & Engels M. 2005. Routine 2D inversion of magnetotelluric data using the determinant of the impedance tensor. *Geophysics 70*, G33–G41.

Pirli M., Schweitzer J., Ottemöller L., Raeesi M., Mjelde R., Atakan K., Guterch A., Gibbons S.J., Paulsen B., Dębski W., Wiejacz P. & Kværna T. 2010. Preliminary analysis of the 21 February 2008 Svalbard (Norway) seismic sequence. *Seismological Research Letters 81*, 63–75.

Pollack H.N. & Chapman D.S. 1977. On the regional variation of heat flow, geotherms, and lithospheric thickness. *Tectonophysics 38*, 279–296.

Simpson F. & Bahr K. 2005. *Practical magnetotellurics*. Cambridge: Cambridge University Press.

Siripunvaraporn W. & Egbert G. 2000. An efficient data-subspace inversion method for 2-D magnetotelluric data. *Geophysics 65*, 791–803.

Slagstad T., Balling N., Elvebakk H., Midttømme K., Olesen O., Olsen L. & Pascal C. 2009. Heat-flow measurements in Late Palaeoproterozoic to Permian geological provinces in south and central Norway and a new heat-flow map of Fennoscandia and the Norwegian–Greenland Sea. *Tectonophysics 473*, 341–361.

Smirnov M., Korja T., Dynesius L., Pedersen L.B. & Laukkanen E. 2008. Broadband magnetotelluric instruments for near-surface and lithospheric studies of electrical conductivity: a Fennoscandian pool of magnetotelluric instruments. *Geophysica 44*, 31–44.

Smirnov M.Y. 2003. Magnetotelluric data processing with a robust statistical procedure having a high breakdown point. *Geophysical Journal International 152*, 1–7.

Smirnov M.Y. & Pedersen L.B. 2009. Magnetotelluric measurements across the Sorgenfrei–Tornquist Zone in southern Sweden and Denmark. *Geophysical Journal International 176*, 443–456.

Spichak V. & Manzella A. 2009. Electromagnetic sounding of geothermal zones. *Journal of Applied Geophysics 68*, 459–478.

Tikhonov A. 1950. On determining electrical characteristics of the deep layers of the Earth's crust. *Doklady 73*, 295–297.

Treiman A.H. 2012. Eruption age of the Sverrefjellet volcano, Spitsbergen Island, Norway. *Polar Research 31*, article no. 17320, doi: http://dx.doi.org/10.3402/polar.v31i0.17320

Vågnes E. & Amundsen H.E.F. 1993. Late Cenozoic uplift and volcanism on Spitsbergen: caused by mantle convection? *Geology 21*, 251–254.

Viljanen A., Pirjola R. & Amm O. 1999. Magnetotelluric source effect due to 3D ionospheric current systems using the complex image method for 1D conductivity structures. *Earth, Planets and Space 51*, 933–945.

Vogt P.R. & Sundvor E. 1996. Heat flow highs on the Norwegian–Barents–Svalbard continental slope: deep crustal fractures, dewatering, or memory in the mud? *Geophysical Research Letters 23*, 3571–3574.

Zhang P., Roberts R. & Pedersen L. 1987. Magnetotelluric strike rules. *Geophysics 52*, 267–278.

Citation: *Polar Research* 2015, *34*, 26766, http://dx.doi.org/10.3402/polar.v34.26766